RESEARCH ARTICLE | MARCH 19 2024

The effect of intrinsic magnetic order on electrochemical water splitting

Emma van der Minne ; Lucas Korol ; Lidewij M. A. Krakers ; Michael Verhage ; Carlos M. M. Rosário ; Thijs J. Roskamp ; Raymond J. Spiteri ; Chiara Biz ; Mauro Fianchini ; Bernard A. Boukamp ; Guus Rijnders ; Kees Flipse ; Jose Gracia ; Guido Mul ; Hans Hilgenkamp ; Robert J. Green ; Gertjan Koster ; Christoph Baeumer

Appl. Phys. Rev. 11, 011420 (2024)
https://doi.org/10.1063/5.0174662

Applied Physics Reviews ARTICLE pubs.aip.org/aip/are

The effect of intrinsic magnetic order on electrochemical water splitting

Cite as: Appl. Phys. Rev. **11**, 011420 (2024); doi: 10.1063/5.0174662
Submitted: 1 September 2023 · Accepted: 16 February 2024 ·
Published Online: 19 March 2024

View Online Export Citation CrossMark

Emma van der Minne,[1,a)] Lucas Korol,[2] Lidewij M. A. Krakers,[1] Michael Verhage,[3] Carlos M. M. Rosário,[1] Thijs J. Roskamp,[1] Raymond J. Spiteri,[4] Chiara Biz,[5] Mauro Fianchini,[5] Bernard A. Boukamp,[1] Guus Rijnders,[1] Kees Flipse,[3] Jose Gracia,[5] Guido Mul,[6] Hans Hilgenkamp,[1] Robert J. Green,[2,7] Gertjan Koster,[1] and Christoph Baeumer[1,8,a)]

AFFILIATIONS

[1]MESA+ Institute for Nanotechnology, Faculty of Science and Technology, University of Twente, Enschede 7500AE, The Netherlands
[2]Department of Physics and Engineering Physics, University of Saskatchewan, Saskatoon, Saskatchewan S7N 5E2, Canada
[3]Molecular Materials and Nanosystems (M2N)—Department of Applied Physics, Eindhoven University of Technology, Eindhoven, The Netherlands
[4]Department of Computer Science, University of Saskatchewan, Saskatoon, Saskatchewan S7N 5E2, Canada
[5]MagnetoCat SL, 03012 Alicante, Spain
[6]Photocatalytic Synthesis (PCS) group, University of Twente, 7522 NB Enschede, The Netherlands
[7]Stewart Blusson Quantum Matter Institute, University of British Columbia, Vancouver, British Columbia V6T 1Z1, Canada
[8]Peter Gruenberg Institute and JARA-FIT, Forschungszentrum Juelich GmbH, Juelich 52425, Germany

[a)]**Authors to whom correspondence should be addressed:** e.vanderminne@utwente.nl and c.baeumer@utwente.nl

ABSTRACT

To reach a long term viable green hydrogen economy, rational design of active oxygen evolution reaction (OER) catalysts is critical. An important hurdle in this reaction originates from the fact that the reactants are singlet molecules, whereas the oxygen molecule has a triplet ground state with parallel spin alignment, implying that magnetic order in the catalyst is essential. Accordingly, multiple experimentalists reported a positive effect of *external* magnetic fields on OER activity of ferromagnetic catalysts. However, it remains a challenge to investigate the influence of the *intrinsic* magnetic order on catalytic activity. Here, we tuned the intrinsic magnetic order of epitaxial $La_{0.67}Sr_{0.33}MnO_3$ thin film model catalysts from ferro- to paramagnetic by changing the temperature *in situ* during water electrolysis. Using this strategy, we show that ferromagnetic ordering below the Curie temperature enhances OER activity. Moreover, we show a slight current density enhancement upon application of an external magnetic field and find that the dependence of magnetic field direction correlates with the magnetic anisotropy in the catalyst film. Our work, thus, suggests that both the intrinsic magnetic order in $La_{0.67}Sr_{0.33}MnO_3$ films and magnetic domain alignment increase their catalytic activity. We observe no long-range magnetic order at the catalytic surface, implying that the OER enhancement is connected to the magnetic order of the bulk catalyst. Combining the effects found with existing literature, we propose a unifying picture for the spin-polarized enhancement in magnetic oxide catalysts.

INTRODUCTION

To establish a sustainable energy infrastructure, efficient energy storage systems are of the highest interest to overcome the intermittent nature of renewable energy sources. Green hydrogen is one of the most promising fuels for energy storage and an ideal feedstock for coupling renewable energy with other sectors like the chemical and the steel industries.[1,2] While alternative and innovative technologies are currently being explored,[3,4] the main predicted production routes of green hydrogen rely on alkaline water electrolyzers and proton exchange membrane electrolyzers.[5,6] However, water electrolysis suffers from sluggish kinetics in the oxygen evolution reaction (OER).[7–9] This might be connected to the fact that the reactants, OH^- or H_2O, are diamagnetic, but the final product, triplet O_2, is paramagnetic.[10,11]

Accordingly, recent theoretical investigations suggest that the spin polarized orbital configurations in ferromagnetic bonds increase OER efficiency by promoting the generation of triplet oxygen by

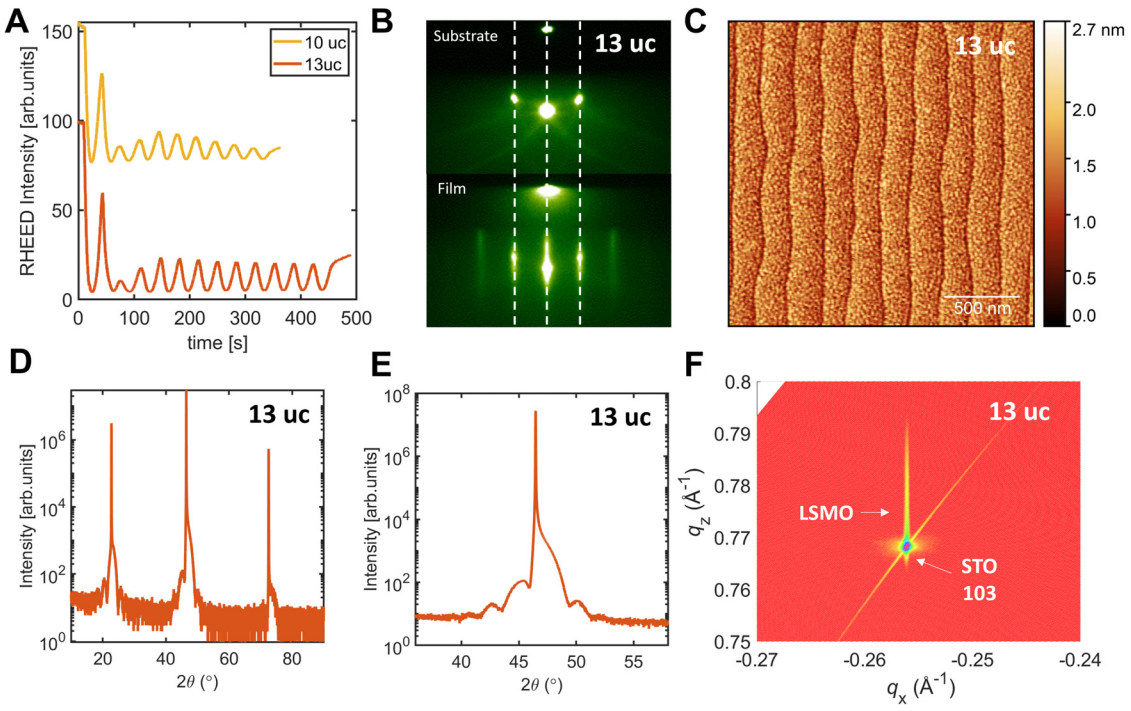

FIG. 1. RHEED and x-ray diffraction of $La_{0.67}Sr_{0.33}MnO_3$ thin films. (a) RHEED intensity during growth of the 10 and 13 uc thick films, with clear oscillations indicating a 2D layer-by-layer growth. (b) RHEED diffraction pattern of the substrate and 13 uc thick film. The equal distance between diffraction spots indicates epitaxial growth. The slight elongation of the spots indicates roughening of the film. (c) AFM image of the 13 uc thick film. (d) Wide 2θ–ω scan of the 13 uc thick film which reveals a single phase of 001 $La_{0.67}Sr_{0.33}MnO_3$. (e) 2θ-ω scan of the 002 $SrTiO_3$ peak of the 13 uc thick film with pronounced Laue fringes. (f) Reciprocal space map of the 103 peak of $SrTiO_3$. As the film peak lies along the same value of q_x as the substrate, the film is fully strained on the substrate.

quantum spin-exchange interactions (QSEIs) and intrinsic spin filtering through exchange splitting of the energy levels in the conduction band of a magnetic material.[10–14] From the orbital physics of correlated electrons, it is hypothesized that maximum OER activity can be obtained at catalytic surfaces with dominant metallic ferromagnetic behavior.[13,14]

Following this idea, multiple experimental studies reported a positive effect of external magnetic fields on OER activity of ferromagnetic catalysts, suggesting several possible explanations.[10,15–24] An increase in spin polarization at the active sites was suspected to reduce the charge transfer resistance at the electrode–electrolyte interface and increase spin selective adsorption.[10,20,24] The removal of domain walls may reduce domain wall scattering and, thus, lower the magnetoresistance and increase the amount of ferromagnetically coupled reactive sites.[18,19] An increase in the ferromagnetic exchange field between antiferromagnetic or paramagnetic catalyst surfaces and ferromagnetic subsurface layers can increase the extent of spin order at the reaction sites.[21,22] Finally, the magnetoresistance effect may increase the activity by decreasing the electronic resistance in the catalyst.[11] From the lack of significant changes in OER enhancement on purely paramagnetic catalysts, it was hypothesized that the effects of Lorentz and Kelvin forces can be excluded as dominant factors for magnetic field enhanced OER activity.[16,17,25]

Although it has been shown that *external* field application on open-shell catalysts can enhance OER activity, it remains a challenge to investigate the influence of the *intrinsic* magnetic order in catalysts. Initial attempts to study the effects of intrinsic magnetic order have shown that a higher saturation magnetization,[26,27] the occurrence of spin channels,[28] a higher spin magnetic moment on the active sites,[29–32] and the introduction of ferromagnetism[30] can enhance either the OER activity directly, or its response to magnetic field exposure. However, to date, these changes in magnetic order were accompanied by a change in either the composition, the crystal structure, or the crystal symmetry of the catalyst such that it remains a challenge to pinpoint the observed effects to the intrinsic magnetic order.

In this article, we introduce a strategy to vary the magnetic order without applied magnetic field during catalysis and without changing the crystal structure. We employed epitaxial $La_{0.67}Sr_{0.33}MnO_3$ thin films grown by pulsed laser deposition[33] as model catalysts with a Curie temperature (T_c) slightly above and below room temperature. This enabled us to change the magnetic order of the catalyst from ferromagnetic to paramagnetic *in situ* during water electrolysis by changing the temperature. At T_c, a change in the catalytic activity is expected, which is connected to the disturbance of the inter-atomic exchange interactions due to thermal fluctuations, also known as the Hedvall effect, as observed for a range of other catalytic processes.[34] Generally, one expects a decrease in current density with decreasing temperature because of smaller thermal energy. By comparing the ferromagnetic and paramagnetic films, we show that for ferromagnetic films, the current densities below the Curie temperature were higher than expected if only temperature dependent effects are considered. This indicates that the presence of ferromagnetic ordering below the

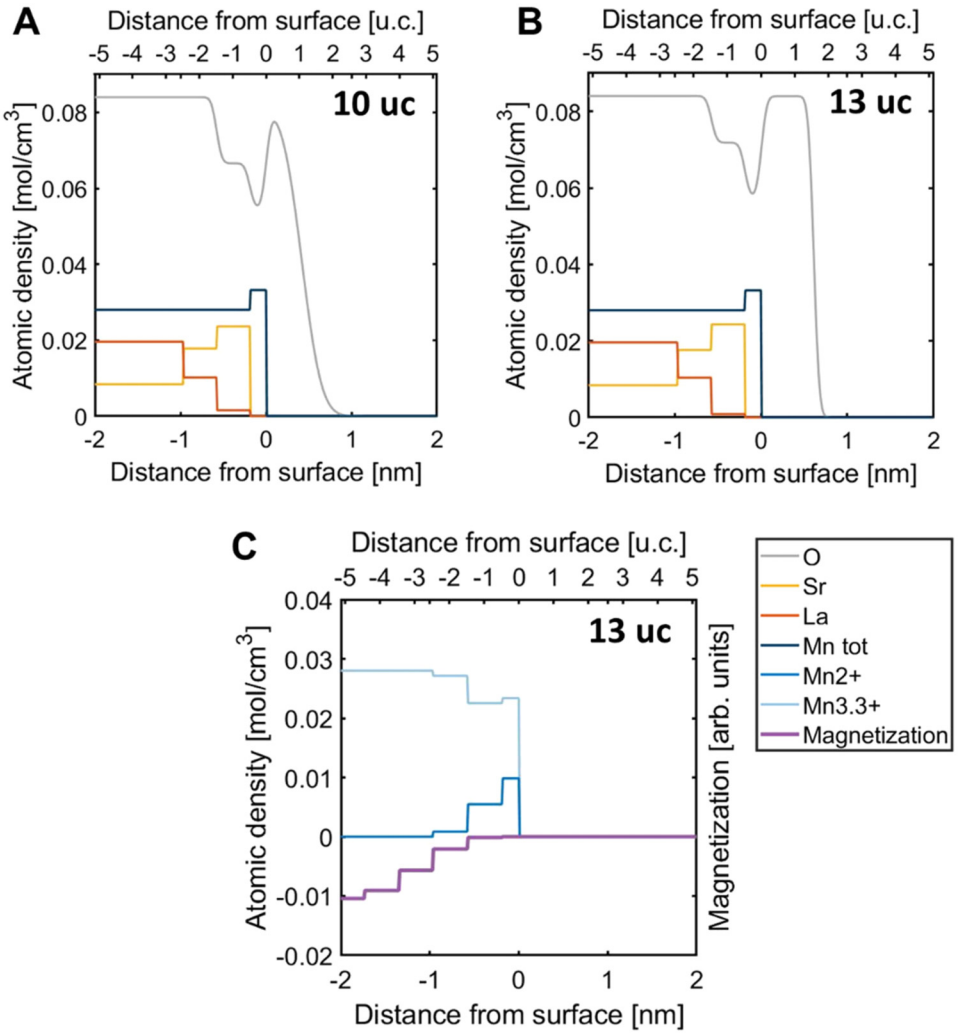

FIG. 2. Unit-cell resolved model obtained from resonant x-ray reflectivity measurements of the films which shows the atomic density of the different elements O, La, Sr, and Mn (total or split up between Mn^{2+} and $Mn^{3.3+}$) as a function of the distance from the surface (see methods for further information) for a (a) 10 uc thick $La_{0.67}Sr_{0.33}MnO_3$ film (b) 13 uc thick $La_{0.67}Sr_{0.33}MnO_3$ film. Measurements were performed at 150 K. (c) Unit-cell resolved model obtained from resonant circular polarized x-ray reflectivity measurements which shows magnetization in the surface region of the film as a function of the distance from the surface. Magnetization is shown alongside the depth dependent atomic density of the Mn species. Magnetization was obtained under a field of 0.6 T at 300 K and is given in arbitrary units.

Curie temperature, i.e., the intrinsic magnetic order, indeed enhances OER activity.

The importance of ferromagnetic order is further demonstrated by an enhancement of OER activity for the same ferromagnetic film upon alignment of magnetic domains with an external magnetic field. We show a correlation between the magnetic anisotropy in our catalyst and the external magnetic field enhancement. Our work, thus, suggests that both the intrinsic magnetic order in $La_{0.67}Sr_{0.33}MnO_3$ films and the magnetic domain alignment upon external field exposure increase the catalytic activity. Moreover, the long-range magnetic order at the catalytic surface is strongly suppressed, implying that the OER enhancement is related to the magnetic ordering of the catalyst bulk, rather than lateral long-range order in the surface layer. Combining our observations with existing literature, we propose a unifying picture for the spin-polarized enhancement in magnetic oxide catalysts.

RESULTS AND DISCUSSION

To study the effects of intrinsic magnetic order, one needs a model system in which physical material properties can be changed without changing composition or crystal structure. Epitaxial thin films, in which highly controlled synthesis helps fine-tune physical properties and electrochemical functionality while maintaining composition and structure, have emerged as an ideal platform to identify structure–function relationships at the atomic level.[35,36] Here, we selected $La_{0.67}Sr_{0.33}MnO_3$ which is a half metal at room temperature associated with a ferromagnetic double exchange mechanism from (intra- and inter-atomic) QSEI.[37,38] Epitaxial thin films of this material enable control of the magnetic properties through the thickness of the film. We utilized this property to tune the Curie temperature similar to the approach described in Ref. 33. Using this approach, we were able to obtain a film in which we could change the magnetic order during OER by changing the temperature. Moreover, we use the strain induced magnetic anisotropy in the film to further investigate the effect of domain alignment and the magnitude of the magnetization in our films.

We synthesized epitaxial thin $La_{0.67}Sr_{0.33}MnO_3$ films of 10- and 13-unit cell (uc) thickness, using pulsed laser deposition (PLD) parameters similar to Ref. 33. For all films, the growth proceeds in a two-

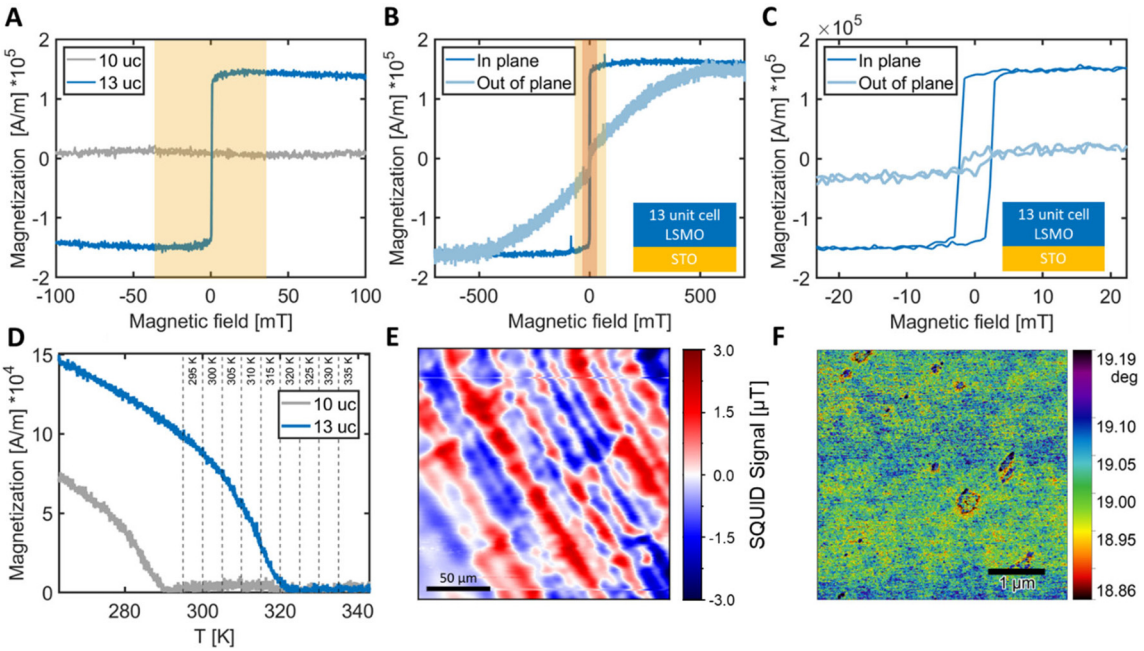

FIG. 3. Magnetic properties of $La_{0.67}Sr_{0.33}MnO_3$ thin films with a thickness of 10 and 13 uc. (a) In-plane magnetic hysteresis loops measured at 300 K. The diamagnetic contribution to magnetization (not shown) has been attributed to the substrate and has been subtracted. The colored area indicates the in-plane magnetic field applied during electrocatalytic experiments described below. (b) In-plane and out-of-plane magnetic hysteresis loops of the 13 uc $La_{0.67}Sr_{0.33}MnO_3$ film obtained under similar conditions as (a). Colored areas indicate the in-plane (orange) and out-of-plane (yellow) fields applied during electrocatalytic experiments. (c) Zoom in of the hysteresis loops shown in (b). (d) Temperature dependent magnetization curve measured at 10 mT. All samples were cooled in this field to 20 K before measurement. The dotted lines indicate the temperatures at which electrochemical measurements were performed. (e) Scanning SQUID microscopy measurement performed at 4.2 K on a 13 uc thick film. (f) MFM measurements obtained at room temperature on a 13 uc thick film. The large features are due to crosstalk from the topography shown in the supplementary material, Fig. 2. The differences in the background indicate inhomogeneity in the magnetic behavior.

dimensional (2D) layer-by-layer manner, as demonstrated by *in situ* reflection high energy electron diffraction [RHEED, Figs. 1(a) and 1(b)], and the resulting surface morphologies exhibit the characteristic vicinal step-terraced structure also observed for the substrate surface [Fig. 1(c)] with small corrugations/islands/decorations on each terrace, which we have shown in Ref. 39. Clear RHEED oscillations during growth indicate the intended thicknesses of 10 and 13 uc [Fig. 1(a)], further confirmed by x-ray reflectivity (XRR), which revealed thicknesses of ∼3.6 and ∼4.8 nm, respectively (supplementary material, Fig. 3). X-ray diffraction measurements reveal a single $La_{0.67}Sr_{0.33}MnO_3$ 001 phase [Fig. 1(d)]. Moreover, the existence of clear Laue fringes indicates a high bulk crystalline quality of the film [Fig. 1(e)]. Reciprocal space mapping confirms coherent strain to the substrate [Fig. 1(f)].

To further investigate the surface structure in our $La_{0.67}Sr_{0.33}MnO_3$ films, resonant x-ray reflectivity (RXR) measurements were performed. Using this technique, the depth dependence of the atomic densities of each of the components in a thin film can be probed.[40] From the obtained unit-cell resolved stoichiometry of the surface [as shown in Figs. 2(a) and 2(b)], we observe that both films have a similar bulk and surface stoichiometry, are B-site terminated, and have Sr enrichment and La deficiency at the surface (similar to Ref. 41). Moreover, a clear indication for oxygen vacancies at the surface is found, which could be the reason for the Mn^{2+} formation shown in Fig. 2(c).

We explored the magnetic properties of the $La_{0.67}Sr_{0.33}MnO_3$ films *ex situ* using vibrating scanning magnetometry (VSM), scanning superconducting quantum interference device (SQUID) microscopy, and magnetic force microscopy (MFM) (Fig. 3). We observe room temperature ferromagnetic behavior with a saturation magnetization of 1.6×10^5 A/m, equal to approximately 1 μ_B/Mn atom, and a H_C of ∼3 mT for the 13 uc film as both a clear hysteresis loop and a T_c of ∼322 K were found. For the 10 uc film, we observe room temperature paramagnetic behavior because no hysteresis loop is observed due to a T_c of ∼290 K. We, thus, successfully prepared two films with different magnetic properties while maintaining crystal structure and stoichiometry in the bulk and only slightly changing the surface chemical composition.

Moreover, as seen in Fig. 3(b), the external magnetic response of the ferromagnetic film is anisotropic. A magnetic easy axis is found along the in-plane direction of the film, which was expected due to the tensile strain induced by the substrate.[42] A distinct domain structure with large domains along one direction is observed for the 13 uc film at low temperature and zero field as shown in Fig. 3(e). However, room temperature MFM measurements reveal a spatial inhomogeneity in the magnetic behavior reflected by the inhomogeneity in the background of Fig. 3(f). We hypothesize that this is due to the formation of a mixed

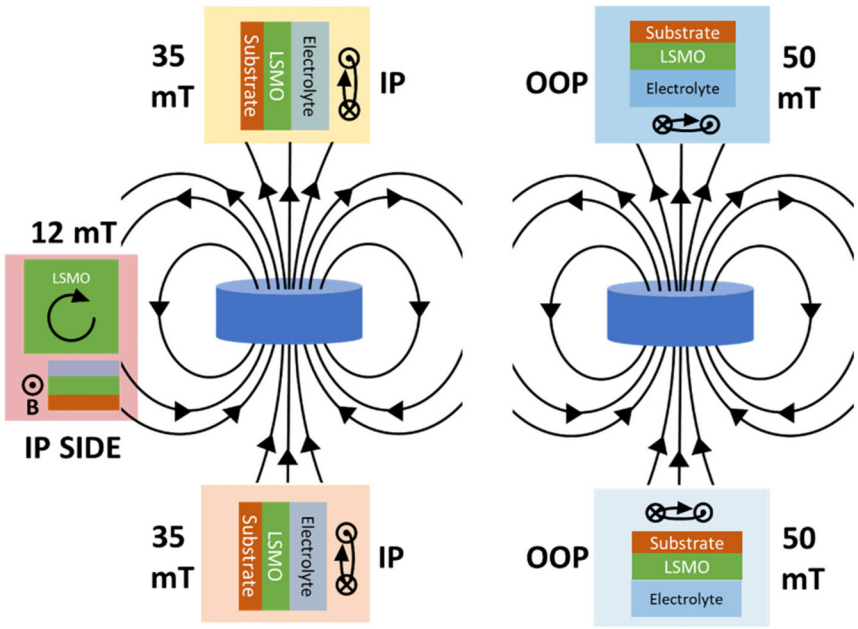

FIG. 4. Schematic of the different field directions during external field application experiments. The direction of the rotation of the sample is shown alongside the relative orientation of the sample to the field lines of the magnet where IP and OOP stand for the configuration where the field lines at the sample are, respectively, parallel or perpendicular to the surface. The applied field strengths of 35 mT for the in-plane directions and 50 mT for the out-of-plane directions are indicated for each of the directions. "IP side" is a special case, where the sample was placed at the side of the magnetic instead of being placed at one of the poles (normal IP and OOP case). Here, the field strength is only 12 mT at the sample.

phase, consisting of a ferromagnetic-like matrix with a range of different long spin correlation lengths containing local defects. Similar behavior has been reported previously for $La_{0.67}Sr_{0.33}MnO_3$.[43] These defects may be of a paramagnetic nature. This behavior is further supported by the trend of the resistivity curve with temperature [supplementary material, Fig. 1(b)], which can only be explained if a competition exists between ferromagnetic (FM) metallic domains and paramagnetic (PM) regions at elevated temperatures, as previously described for similar manganite oxides.[39,44,45] These paramagnetic domains can be a reason for the low saturation magnetization compared to the low temperature value for bulk $La_{0.67}Sr_{0.33}MnO_3$ of 2.5 μ_B/Mn.

Having established the physical properties of our model catalysts, we now turn to electrochemical investigation. We review the magnetic-field dependent activity first, followed by the assessment of the effect of the intrinsic magnetic order. Cyclic voltammetry measurements were performed, both in the absence and presence of an applied external magnetic field in different in-plane and out-of-plane directions (see Fig. 4 and methods for details). The presence (absence) of systematic changes between the activity with and without in-plane applied magnetic field for ferromagnetic (paramagnetic) catalysts indicates that the activity enhancement is linked to the increase in magnetization in the ferromagnetic film upon external field application [Figs. 5(a), 5(b), 5(e), and 5(f) and supplementary material, discussion A]. Due to ageing and scattering, the effect of the out-of-plane field exposure could not be distinguished [Figs. 5(c), 5(d), 5(g), and 5(h)], a point to which we will return below.

To further separate the effects of the external field application from ageing or scattering effects, chronoamperometry measurements

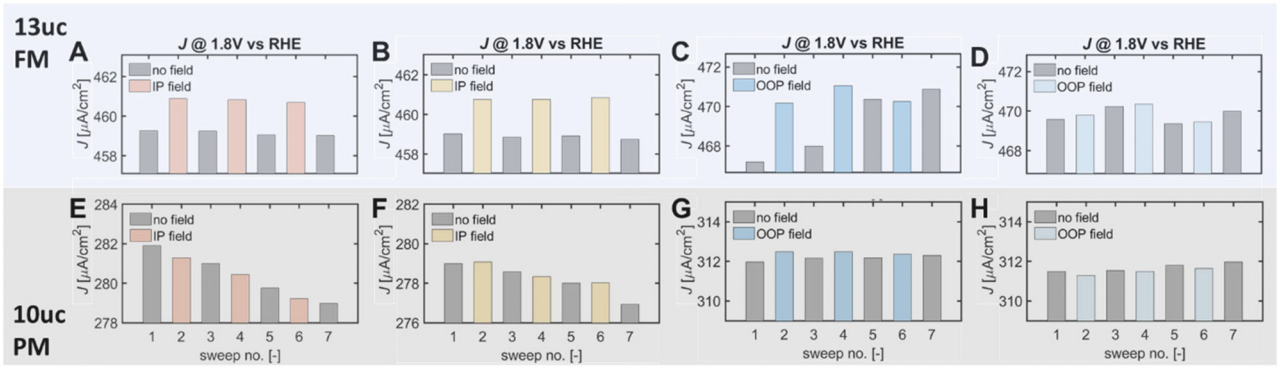

FIG. 5. (a)–(h) Current densities obtained from cyclic voltammetry measurements (see the supplementary material, Fig. 4) at an potential of 1.8 V vs RHE for different sweeps. Top row: 13 uc thick $La_{0.67}Sr_{0.33}MnO_3$ film. Bottom row: 10 uc thick $La_{0.67}Sr_{0.33}MnO_3$ film. Colored bars indicate the presence of an external magnetic field during the sweep, while gray bars indicate sweeps which were done without the presence of a field. The color of the bar represents the direction of the field and corresponds to the colors indicated in Fig. 4.

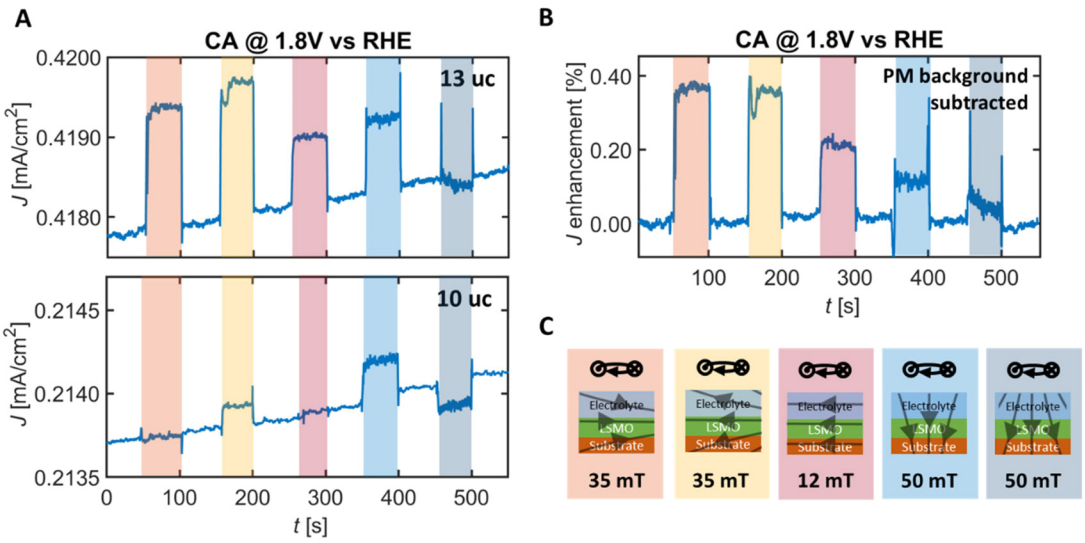

FIG. 6. (a) Chronoamperometry measurement at an potential of 1.8 V vs RHE for a 13 uc and a 10 uc thick $La_{0.67}Sr_{0.33}MnO_3$ film during which an external magnetic field was applied in different directions. The colored bars indicate the intervals during which the field was applied. The color of the bar represents the direction of the field and corresponds to the colors indicated in Fig. 4. (b) Normalized current density enhancement due to ferromagnetic interactions after paramagnetic background subtraction. (c) Schematic drawing of the field lines in the samples and in the electrolyte. The arrow on top indicates stirring direction.

were performed at 1.8 V vs RHE. External fields were applied in different in-plane and out-of-plane directions. Again, an enhancement in current density was observed for the ferromagnetic materials upon in-plane field application [Fig. 6(a)]. However, for the behavior linked to the out-of-plane fields, the change in current density depends heavily on the direction of the field lines perpendicular to the sample surface [Figs. 6(a) and 6(c)]. Moreover, the paramagnetic sample showed clearly distinguishable changes in current density upon magnetic field exposure in certain directions contrary to previously published results.[10,16,25] This behavior and possible origins are discussed in more detail in the supplementary material, discussion B. In these measurements, ageing effects can be seen again as the current density in the periods between magnetic field application slightly increases over time.

To differentiate the effect of the changes in internal magnetic order through domain alignment from other effects also at play for the paramagnetic sample, the paramagnetic background as well as ageing induced effects were subtracted from the response of the ferromagnetic film [Fig. 6(b)]. Interestingly, an enhancement was found in all field directions for the renormalized data, implying that domain alignment of the FM sample is connected to the activity enhancement. The current increase is more than two times higher in the in-plane direction than in the out-of-plane direction (~0.4% and 0.1%, respectively), implying an anisotropic enhancement: A small field along the in-plane direction has a larger effect on OER activity than a larger field applied in the out-of-plane direction. As discussed previously, the $La_{0.67}Sr_{0.33}MnO_3$ thin films have a magnetic easy axis along the in-plane direction and a magnetic hard axis along the out-of-plane direction. Application of external in-plane fields will, thus, increase the total magnetization and remove domain walls to a larger extent than out-of-plane fields. This anisotropy in the magnetic response to an external field can, thus, explain the anisotropy of the activity enhancement, indicating that the enhancement is connected to changes in the magnetic structure of the films. Comparing the magnitude of the enhancement to the increment in magnetoresistance at these field strengths, which is less than ~0.05% [supplementary material, Fig. 1(a)], we exclude the change in magnetoresistance as a dominant factor for magnetic field enhanced OER activity in this system.

To further verify that the differences in the enhancement of the current densities upon external field application between the paramagnetic and ferromagnetic samples are induced by a difference in magnetic order and not induced by the sample geometry, we performed similar chronoamperometry measurements with and without applied magnetic field at different temperatures for the room temperature ferromagnetic 13 uc sample. As shown in Figs. 7(a) and 7(b), the response of the 13 uc sample above T_C is similar to the behavior of the paramagnetic 10 uc, while the expected enhancement for the ferromagnetic sample can be observed below T_c. This further confirms that the alignment of FM domains induces the enhancement of OER in the external magnetic field measurements.

Although we have, thus, shown that changing the total magnetization in the catalyst can enhance OER activity, we have not yet touched upon the key point of investigating the influence of the intrinsic magnetic order in catalysts without the application of an external field. For this purpose, we explored the Hedvall effect in the OER and changed the intrinsic magnetic order *in situ*. We performed OER measurements at different temperatures. These temperatures are indicated by the vertical lines in Fig. 3(d). As can be seen, the FM sample changes from FM to PM in this temperature range (for more information, see methods).

For all samples, a decreasing activity with decreasing temperature was observed (Fig. 7 and supplementary material, Fig. 5). This loss in current density J is expected because lowering the temperature lowers

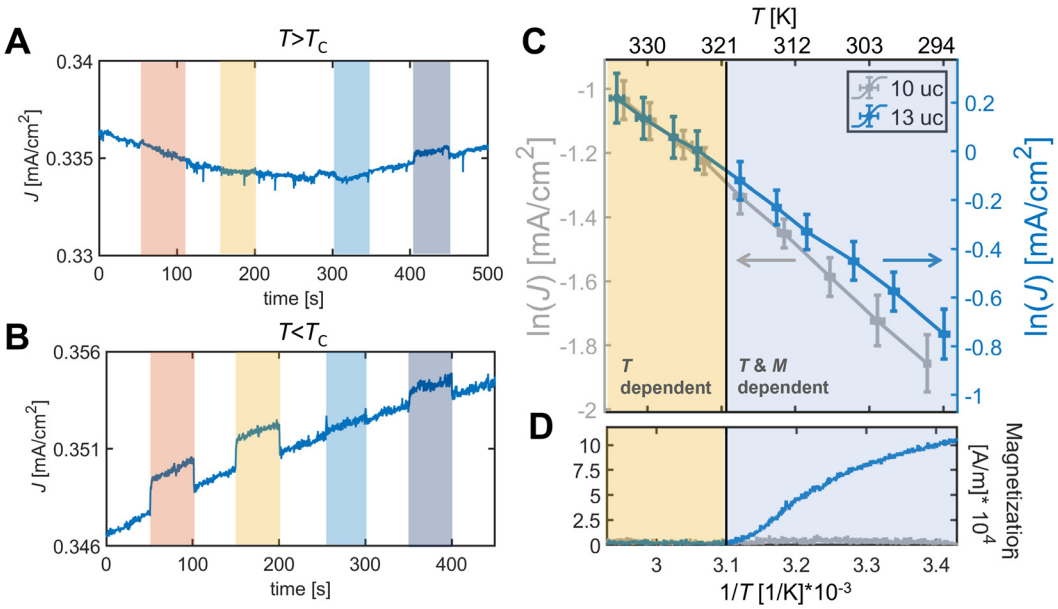

FIG. 7. Chronoamperometry measurement at a potential of 1.69 V vs RHE for a 13 uc $La_{0.67}Sr_{0.33}MnO_3$ film during which an external magnetic field was applied in different directions both above (a) and below (b) the curie temperature of this film. (c) Plot of the natural logarithm of the current density vs the inverse of the temperature obtained for a ferromagnetic (13 uc) and a paramagnetic (10 uc) $La_{0.67}Sr_{0.33}MnO_3$ film at an *iR* corrected potential of 1.8 V vs RHE. The plot is shown alongside the magnetization (c) of the films in the same temperature range. Error bars indicate the estimated errors from temperature fluctuations, sample ageing over measurement time, and reading of *iR*-corrected potentials.

the thermal energy, lowering the reaction rate of the OER. Simplifying the Butler–Volmer equation using the Tafel approximation at high potentials and neglecting diffusion limitations gives[46]

$$\ln J = \ln J_o + \alpha_f F \eta \frac{1}{k_B T}, \quad (1)$$

for the exchange current density J_o, the transfer coefficient of the overall forward reaction α_f, Faraday constant F, overpotential η, and Boltzmann constant k_B. However, the exact temperature-dependent behavior may deviate from Eq. (1) because multiple effects like water adsorption and dissociation, the nature of adsorbed species, and movement of oxygen vacancies or interstitials in the catalyst can also be influenced by temperature.[47] While this complicates identification of magnetic-order-effects, a comparison between 10 uc and 13 uc samples enables differentiating different effects, because the chemical composition is similar for both samples and the purely temperature dependent electrochemical effects should be similar. On the contrary, a change in intrinsic magnetic order occurs for the 13 uc thick film in this temperature range ($T_C \approx 321$ K), whereas the 10 uc film is paramagnetic over the entire temperature range.

The difference in electrical resistance between these two films resulted in differences in absolute activity, necessitating a comparison of the activity trends with varying temperature. We plot $\ln J$ vs $\frac{1}{T}$ for both films in an Arrhenius plot [Fig. 7(c)], using offset y-axes to account for the overall activity differences, where the slope is proportional to η [Eq. (1)]. For the paramagnetic 10 uc film, we find the expected almost linear decrease in $\ln J$ with $\frac{1}{T}$. However, for our ferromagnetic film, there are competing effects for $T < T_c$, reflected by the upward deviation of the slope of the 13 uc sample for $T < T_c$ (blue region) compared to the paramagnetic 10 uc sample, whereas for $T > T_c$ (yellow region), the slopes of both samples are similar [Fig. 7(c)]. The positive change in slope implies a decreased overpotential or a change in transfer coefficient, increasing the OER activity. We observe an enhancement of ~35% compared to the expected current density without ferromagnetic order (see the supplementary material, Fig. 6 for derivation). Additional control measurements using chronoamperometry measurements during cooling verified this behavior as can be seen in the supplementary material, Fig. 7(a). Moreover, we find that when changing the T_C of the 13 uc sample, the onset of the upward deviation occurs at the new T_C, further confirming that the deviation is induced by the occurrence and continuous increase in the ferromagnetic order [supplementary material, Fig. 7(c)]. As discussed in the supplementary material, discussion C and shown in the supplementary material, Fig. 8, we identify that the effect results from changes in the charge transfer and uncompensated resistances. The role of the charge transfer resistance is in line with the hypothesis that the magnetic order can decrease the charge transfer resistance during OER. The additional effect of the uncompensated resistance may be connected to an increase in conductivity due to double exchange interactions arising below T_C. Moreover, sample degradation, surface restructuring and changes in the double layer capacitance with temperature cannot explain the observed effects. We can, thus, conclude that the occurrence and continuous increase in the ferromagnetic order with decreasing temperature induces the relative current density enhancement below T_C.

To summarize, we have shown a relative current density increase during OER upon changing the magnetic properties of $La_{0.67}Sr_{0.33}MnO_3$ thin film catalysts. The combination of effects shown in the temperature-dependent OER activity measurements for a ferromagnetic

catalyst and the effects shown while exposing the same ferromagnetic catalysts to an external magnetic field during OER validate that the enhancement is primarily induced by the changes in magnetic order in the catalyst.

The comparably small enhancement shown upon external magnetic field application (see the supplementary material, Table 4 for a detailed comparison to prior works) may be explained by the small applied external field, small coercivity and low saturation magnetization of the $La_{0.67}Sr_{0.33}MnO_3$ films at 300 K. Most importantly, the difference between saturation and initial magnetization in $La_{0.67}Sr_{0.33}MnO_3$ films is comparatively small due to a small coercive field, large domains, and the presence of paramagnetic regions, which lowers the increment in magnetization upon alignment, as discussed in depth by Ge *et al.*[18] The increments induced by the occurrence of intrinsic magnetic order are more comparable in magnitude to the enhancements found in previous literature. This further confirms our understanding that the total possible enhancement is a combined effect of the PM to FM transition and the alignment of the domains. Depending on the material choice (and thus, the remanent magnetization, domain structure, coercive fields), the ratio of these two increments will change. Moreover, both the effects of domain alignment and a change in magnetic order could be influenced by the existence of a magnetic dead-layer, in which any long-range magnetic order is diminished. Our epitaxial model system is a suitable platform to further investigate the effect of such dead-layers, similar to previous studies focusing on the surface properties of $La_{0.67}Sr_{0.33}MnO_3$ films.[41,48,49]

To further investigate where the magnetic order resides in our $La_{0.67}Sr_{0.33}MnO_3$ films, we again use RXR in vacuum. Using left- and right-circularly polarized light, a depth profile of the magnetization can be obtained from the best fit of the asymmetric spectra [Fig. 2(c)] (for more information, see methods).[50,51] We found that the net magnetization in the top 1.5 uc of the 13 uc thick $La_{0.67}Sr_{0.33}MnO_3$ film is zero and that the magnetization is quenched in the subsurface layer up to 4 uc, even under an applied field. This decreased magnetization is likely connected to the off-stoichiometry discussed above. As these off-stoichiometries likely deteriorate long-range ordered magnetic states, we hypothesize that the 1.5 uc thick surface layer is paramagnetic. Although these measurements were done *ex situ*, the paramagnetic surface layer is likely also present under OER conditions, because the magnetic fields applied in the electrochemical cell are smaller than the fields during RXR measurements.

The lack of lateral long-range magnetic order in the catalyst surface implies that no ordered interaction exists between the long-range ordered spin states of the metal atoms in the film and the reaction intermediates. We can, thus, conclude that the observed OER enhancements due to inter-atomic QSEI are mainly induced by the magnetic order in the bulk of the $La_{0.67}Sr_{0.33}MnO_3$ films. Still the intra-atomic QSEI is always present and persists in the surface layer. The spin-polarization of the adsorbents is, thus, presumably mediated through the out-of-plane QSEI in the paramagnetic surface layer, which is smaller than the ferromagnetic QSEI in the bulk, limiting the efficiency of the OER enhancement.

Based on the findings from the epitaxial $La_{0.67}Sr_{0.33}MnO_3$ thin film model system and considering the range of observations in recent literature, we propose a unifying picture for the spin-polarized OER activity enhancement in oxide catalysts, schematically shown in Fig. 8. The lowest activity is found for a paramagnetic material with no spin channels (left panel).[11,34] Because of the absence of stable spin channels in this catalyst, O–O intermediates with parallel and antiparallel spin alignment can both be formed. The latter do not have optimum inter-site quantum spin exchange interactions and electronic quantum correlations are not optimum for the thermodynamic overpotential.

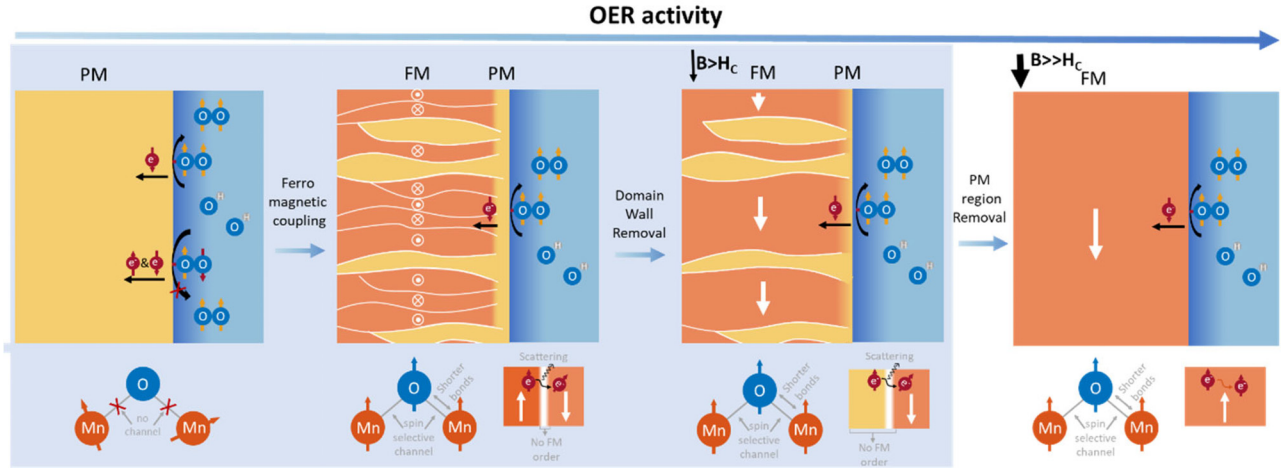

FIG. 8. Proposed mechanism for spin-polarized OER activity enhancement in epitaxial $La_{0.67}Sr_{0.33}MnO_3$ thin films. In the left panel, we show a fully paramagnetic catalyst layer, which corresponds to our 10 uc sample for the entire T range investigated here and the 13 uc sample at $T > T_C$. In the second panel, the catalytic film is made up of a ferromagnetic matrix with domains in which paramagnetic regions are embedded. Moreover, a paramagnetic surface layer is present. This state corresponds to the intrinsic magnetic state of our 13 uc film at $T < T_C$. The third panel shows the state of the catalyst after domain removal in the ferromagnetic matrix upon external magnetic field exposure. The right panel shows the ideal state of the 13 uc film after removal of the paramagnetic regions and surface layer, a homogeneous ferromagnetic catalyst. The states achieved in this work are highlighted with a blue square. At the bottom of the image, we show the physical interactions in the film which account for the presence/absence of spin selectivity during adsorption of electrons. The reaction intermediates shown are highly simplified to focus only on the formation of the O–O bond which is the most important bond when considering the spin-polarized OER mechanism as the spin alignment in this bond either blocks or allows the formation of triplet oxygen.[17]

If ferromagnetic ordering comes into play below T_c, a film consisting of a ferromagnetic bulk with small embedded paramagnetic regions and a paramagnetic surface is obtained (Fig. 8, second panel). The ferromagnetic exchange interactions in the matrix induce ordered itinerant spin channels, inducing spin-selective electron mobility. This leads to a higher possibility of the formation of bonded spin-ordered O–O intermediates which in turn increases the OER activity.[11,14] Moreover, the QSEI associated with the spin orbital ordering lowers the interatomic repulsions, which lead to shorter metal-oxygen bonds, which in turn may act favorably on the reaction intermediate binding energies and thereby decrease the charge transfer resistance during OER.[14] All of these aspects facilitate the generation of triplet O_2 molecules for ferromagnetic thin film catalysts.[14] However, the described ferromagnetic film still contains domains and domain walls. The domain walls induce electron scattering, effectively lowering spin selective transport.[15,19] Moreover, the presence of domain walls and paramagnetic regions lowers the amount of ferromagnetic reaction sites[19] and the paramagnetic surface lowers the effectiveness of the interaction between the ferromagnetic domains in the bulk of the film and the adsorbents.

Upon domain wall removal under the influence of an external magnetic field, a uniform ferromagnetic matrix is obtained (Fig. 8, third panel). The removal of domains lowers the amount of domain wall scattering and increases the amount of long-range magnetically ordered reaction sites. Moreover, the exchange field between ferromagnetic bulk and paramagnetic surface layer becomes stronger, which may become thinner as a result, enhancing the interaction between the ferromagnetic layer and the adsorbents.[21] The effectiveness of domain alignment depends on the strength and direction of the magnetic field and the remanent magnetization of the catalyst. However, as paramagnetic regions remain, OER activity is still not optimal. The application of higher external fields could further improve the performance, by increasing the net magnetic moment in the paramagnetic regions until saturation is achieved and the paramagnetic regions and surface layer are completely removed (Fig. 8, right panel).[10,20] This effect could explain the differences in activity enhancement between this work and the results shown in Ref. 24, where much higher fields were applied. This fully ferromagnetic state is not accessible in our model system using realistic fields. Further research, thus, needs to be done to verify OER enhancement in such a fully long-range ordered electrocatalyst.

This picture of magnetic-order related OER enhancement covers the effects of intrinsic magnetic order (FM vs PM), enhancement in reactivity of individual sites due to long-range magnetic order (QSEI), global activity enhancement by domain wall removal (increased number of highly active sites, improved spin selective transport) and the possibility of sample-specific limitations in the observed effects. It is further compatible with the effect of spin pinning layers,[21] where a nominally paramagnetic surface layer exhibits spin alignment due to a FM subsurface layer. The same picture may also be adaptable to other spin-sensitive reactions like CO_2 reduction.[52] Other spin-related phenomena like the filling of specific orbitals[53] are not directly included in our picture and the spin-transport mediated activity observed in chiral catalysts may have different origins than the magnetically enhanced OER, although both are related to the paramagnetic properties of the product.[54–56] The connection between different spin-induced phenomena in electrocatalysis will remain subject of further development of these emerging fields. Furthermore, future studies may be carried out at higher TRL level to identify hydrogen production efficiency enhancement based on magnetic order of the OER catalyst on electrolyzer scale. Such applications may benefit from design rules derived from our picture. For example, the need for external magnetic fields, which are challenging to include in industrial-scale electrolyzers, may be overcome using spin pinning or single domain particles, which leads to systems similar to the right panel in Fig. 8.

CONCLUSION

In conclusion, we employed epitaxial $La_{0.67}Sr_{0.33}MnO_3$ thin film model catalysts to arrive at a unifying picture of the effects of intrinsic magnetic order and applied magnetic fields on the oxygen evolution reaction. We tuned the magnetic order in the films *in situ* during OER by exploiting the para- to ferromagnetic transition at T_c. Using this strategy, we showed that the presence of ferromagnetic ordering below the Curie temperature enhances OER activity. In the ferromagnetic films, application of external magnetic fields is linked to a further increase in OER activity. Moreover, we observed a correlation between the magnetic anisotropy in our catalyst and the external magnetic field induced OER enhancement. Our work, thus, suggests that both the intrinsic magnetic order in $La_{0.67}Sr_{0.33}MnO_3$ films and externally triggered changes in the magnetic structure affect the catalytic activity of these films. The OER enhancements due to inter-atomic QSEI are found to primarily result from changes in the magnetic order of the bulk of the catalyst, because no long-range magnetic ordering existed at the catalytic surface. To further verify the proposed unifying picture, further research could focus on operando magnetic characterization to directly correlate the magnetic order and interactions in these catalysts with the activity under realistic OER conditions.

METHODS

Pulsed laser deposition

$La_{0.67}Sr_{0.33}MnO_3$ thin films were deposited via reflection high-energy electron diffraction (RHEED)-assisted pulsed laser deposition (PLD) onto B-site terminated and step-terraced $SrTiO_3$ (001) substrates purchased from CrysTec GmbH or Shinkosha Co., Ltd. A stochiometric $La_{0.67}Sr_{0.33}MnO_3$ target was obtained from SurfaceNet. The films were deposited with a laser fluence of 2.0 J cm^{-2} and a frequency of 1 Hz. The deposition was done at an oxygen pressure of 0.266 mbar, and the temperature of the substrate was kept at 750 °C during deposition. The distance between sample and target was kept at 5 cm, and a rectangular mask was used to obtain a laser spot size of 2.24 mm^2. Before deposition, the targets were pre-ablated at 5 Hz. After deposition, the samples were cooled down at 25 °C/min inside the PLD at 100 mbar oxygen pressure. PLD was performed in a vacuum system (TSST) with a base pressure of 5×10^{-8} mbar, equipped with an *in situ* RHEED (Staib instruments) and a KrF excimer laser (Coherent, Inc.) of 248 nm.

Thin film characterization

X-ray diffraction and reflectivity measurements were performed using a Panalytical X'pert pro diffractometer with Cu anode. For the diffractograms, a GE 220 Monochromator was used to obtain Cu-K_α radiation. During the 2θ–ω scans, the detector was operated in 0D mode with an active length of 0.165 mm. A slit of 1/2° was used to shape the beam. Reflectivity measurements were performed using a 1/32° slit. The detector was operated in 0D mode with an active length

of 1.12 mm. The RSM was performed using a Bruker D8 Discover diffractometer with Cu-K_α radiation and an Eiger 2 R 500 K area detector. The detector was kept stationary while operated in 1D mode as an omega rocking curve was performed. A grazing-exit configuration was chosen to obtain narrow diffractograms.

The topography of the grown films was characterized by atomic force microscopy (AFM) using a Veeco Dimension Icon AFM in tapping mode in air. The oscillating cantilever is a Tespa-V2 cantilever (Bruker, Netherlands) with a pure silicon tip with a nominal radius of 20 nm. Images were obtained using the Nanoscope software and treated using the Gwyddion software. First, we align the rows using a polynomial approach, then the data are leveled by mean plane subtraction, finally a polynomial background was subtracted.

Magnetic characterization

VSM measurements were obtained using a DYNACOOL physical properties measurement system (Quantum Design, Germany). All samples were field cooled at 10 mT before measuring temperature-dependent magnetization.

Scanning superconducting-quantum-interference-device (SQUID) microscopy measurements were performed at 4.2 K in a liquid He bath. A superconducting Nb shield is used to shield the sample and SQUID sensor from any external magnetic fields. The SQUID sensor used is extended with a pickup loop having an effective area of approximately 18 μm^2, and scanning is performed under an angle of approximately 15°, making the distance between the pickup loop and sample surface approximately 2–3 μm. The SQUID is a flux-to-voltage transducer, and the measured voltage can be converted to magnetic field by dividing by the (measurement-dependent) flux-to-voltage ratio and the effective area of the pickup loop. Typical flux sensitivities are in the order of 10–20 $\mu\Phi_0/(\mathrm{Hz})^{1/2}$, and the bandwidth is 1000 Hz.[57,58]

Magnetic force microscopy was performed with a CoCr coated Si cantilever, with a spring constant of 2.5 N/m and a resonant frequency around 65 kHz. Prior to imaging, a permanent magnet was used to magnetize the tip for sensitivity of in-plane magnetic fields. A Veeco Dimension AFM III was operated in tapping mode feedback. The image was obtained at 1 Hz scan speed with 512 pixels × 512 lines. The magnetic signal was obtained by a lift mode, with a lift height of 10 nm. Gywddion was used for image processing with plane subtraction and line alignment via means of differences.

Electrochemical characterization

To perform electrochemical experiments with epitaxial thin films on $10 \times 10 \times 0.5\ \mathrm{mm}^3$ single crystal substrates, we used a custom-made adapter to press the sample back side to the Pt plug of a rotating disk electrode (RDE, Pine Research). For further details, see the supplementary material, Fig. 9. 50 nm Pt connections from the sample back side to the front side ensured electrical contact with the $SrTiO_3$ substrate and the epitaxial layers. On the front side, a film area of 7.5 mm diameter was exposed to the electrolyte and sealed using an O-ring (Kalrez, ERIKS, Germany). The RDE shaft was rotated at 1600 rpm. Electrochemical testing was performed using a Biologic SP-300 potentiostat in a 150 ml alkaline-resistant cup with a Pt wire as a counter electrode. Electrochemical impedance spectroscopy (EIS) was conducted with the amplitude of 10 mV. Correction for the cell resistance (*IR* correction) was based on the high-frequency intercept of the real impedance close to open circuit conditions.[59] The electrolyte solution of 0.1 M KOH was prepared by dissolving KOH pellets (Sigma-Aldrich, 99.99%) in Milli-Q water. The electrolyte was O_2-saturated prior to testing for at least 30 min and maintained under an O_2 atmosphere during testing. Electrochemical measurements in the presence of magnetic fields were performed at room temperature unless specified differently. Potentials were referenced to a Hg/HgO reference electrode (C3 Prozess-und Analysentechnik, Germany). The potential of the Hg/HgO was periodically measured against a reversible hydrogen electrode (RHE, HydroFlex, USA) in 0.1 M KOH, with typical values ranging from 883 till 897 mV. For conversion to the RHE scale, we used 890 ± 5 mV. All of the OER testing was performed on a fresh electrode that had not undergone previous testing.

For all samples, we first performed impedance spectroscopy at OCV and cyclic voltammetry (CV) in the double layer region (~1.1–1.2 V vs RHE). At each scan rate, two measurements were taken. After this initial analysis, we performed the steps specified for each measurement presented in this work. The measurement sequence was finished by a repetition of the impedance spectroscopy at OCV and cyclic voltammetry (CV) in the double layer region. For the temperature dependent CV experiments, the measurement specific steps consisted of OER testing using cyclic voltammetry from 1.1 to 1.89 V vs RHE at a scan rate of 10 mV s^{-1}. Three cycles were performed at each temperature. Before performing temperature dependent CV experiments, 10 OER cycles were performed to initialize the samples and reach a more stable performance. For the temperature dependent CA experiments, linear sweep voltammetry at a scan rate of 10 mV s^{-1} was used to sweep up and down the potential before and after chronoamperometry measurements and impedance measurements at elevated potentials. During cooling, we noted down the time whenever the temperature dropped by 1 °C. This was used to determine the data points in the $\ln(J)$ vs $1/T$ graphs in the supplementary material, Fig. 7. Before we applied any external magnetic fields or changed the temperature during CA, we waited until the measured current approached a stable value. CA measurements were complemented with impedance spectroscopy measurements at the same DC potential every 5 min during the CA measurement time.

External magnetic fields were applied using a 1 T permanent disk magnet. The applied field strength depended on the distance between the magnet and the sample and was measured as a function of distance for each of the directions using a flat hall probe in air. For elevated temperature experiments, the electrochemical setup was placed in a heater water bath (see the supplementary material, Fig. 9). The temperature of the solution was measured in close proximity to the working electrode to determine the temperature near the working electrode. After heating to each temperature for the cyclic voltammetry measurements, we waited for approximately 20 min to ensure temperature stabilization. Temperature dependent measurements on the ferromagnetic samples both using cyclic voltammetry and chronoamperometry were duplicated with different samples. External magnetic field measurements on all samples were duplicated on different samples; moreover, for each of the field direction, we repeated the application and removal in a triplicate measurement. The results from this last measurement can be seen in the supplementary material, Fig. 10. An error analysis was performed for temperature dependent measurements on the ferromagnetic samples both using cyclic voltammetry and chronoamperometry and are discussed in the supplementary material, discussion D.

The impedance spectra collected during chronoamperometry measurements were fitted with the equivalent circuits shown in the supplementary material, Fig. 14. Both circuits are made up of an *RQ*/*RC* element to simulate the high frequency response and an *RQ* element to simulate the medium frequency response ($R_{CT}Q_{mid}$) which is suspected to represent the solid–liquid interface. The circuits differ in the last element needed to obtain good fits. For the 10 unit cell sample, another R_3Q_{low} element is needed, which we assume is due to the comparatively higher film resistance, dominating the overall current density. For the 13 unit cell sample, a Finite Length Warburg (FLW) element was used. Such an element is often used to model an electrochemical cell with an RDE due to the negligible diffusion layer induced by fast stirring.[60] For the 13 uc sample, the reaction is not limited by the film resistance, such that diffusion in the liquid and, thus, the Warburg element has to be taken into account. We extract the uncompensated resistance (R_u) and the charge transfer resistance from this complex nonlinear least squares-analysis.

RXR

The resonant x-ray reflectometry (RXR) data were acquired at the resonant elastic and inelastic x-ray scattering (REIXS) beamline of the Canadian Light Source (CLS) in Saskatoon, Canada.[61] The beamline has a flux of 5×10^{12} photons s^{-1} and has a photon energy resolution $\Delta E/E \sim 10^{-4}$. An elliptically polarizing undulator (EPU) is used to give the desired linear and circular polarizations. The experimental chamber was kept below a base pressure of 10^{-9} Torr, and the measurements were taken at a temperature of 300 K. The samples were aligned with their surface normal in the scattering plane, and the reflection-geometry scans were aided by the in-vacuum 4-circle diffractometer. The measurements were performed in the specular reflection geometry with several resonant photon energies at Ti $L_{2,3}$ (∼450–470 eV), Mn $L_{2,3}$ (∼635–660 eV), and La $M_{4,5}$ (∼830–860 eV) resonances, along with multiple non-resonant photon energies. The circular-dichroic magnetic measurements were performed by inserting a permanent magnet array into the sample environment producing a homogenous 0.6 T field, aligning the magnetization in both the film *xy* plane and the measurement scattering plane. The dichroic measurements were then taken solely using the resonant photon energies of the Mn $L_{2,3}$ resonance. A photodiode was used to detect the reflected beam intensity, with the response function of the photodiode determined by directly measuring the synchrotron beam. The measured data were normalized by the incident beam flux and the response function to obtain a quantitative reflectivity spectra.

The modeling of the RXR data was performed using the global optimization of resonant x-ray reflectometry (GO-RXR), a software package recently developed by the QMaX group at the University of Saskatchewan. Tabulated atomic form factors were used for non-resonant energies, while the resonant scattering tensors for elements Ti, Mn, and La were constructed using measured x-ray absorption spectra. For Mn, two different resonant scattering tensors were used—one for Mn^{2+} and one for Mn in stoichiometric $La_{0.7}Sr_{0.3}MnO_3$ (implemented as a weighted linear combination of Mn^{3+} and Mn^{4+} scattering tensors corresponding to $Mn^{3.3+}$). To determine the optical and magneto-optical profiles, a slab model was used that is made up of parametrized layers with defined elements, oxidation states, thicknesses, densities, and roughness. The model parameters are then used to construct an element-specific continuous depth-dependent density profile. The density profile, along with the form factors, is then used to determine the energy- and depth-dependent optical profile. The optical profile is then used to simulate the reflectivity for a given energy, reflection angle, and polarization. To determine the density profile of the 10 and 13 uc $La_{0.67}Sr_{0.33}MnO_3$ samples, the parameters of layer thickness, density, roughness, and Mn oxidation state were optimized while fitting the simulation to the experimental data. To reduce the parameter set, the concentration ratio of Sr and La was fixed to 3:7 throughout the bulk of the film (from the target stoichiometry), but it was allowed to vary near the interface and surface. To determine the magnetic profile of Mn, the nonmagnetic elemental density profile was determined first by optimizing the parameters against an extended sigma-polarized experimental dataset. The magnetic density profile was then fit to the circular polarized data using the asymmetry of the right R_R and left R_L circular polarizations, where $A = (R_L - R_R)/(R_L + R_R)$. We show the experimental RXR data and associated fits of the resonant and non-resonant theta/two-theta reflectivity scans and circular polarized asymmetry scans at different energies in the supplementary material, Figs. 15 and 16. Moreover, the Mn-resonant energy scans and Mn-resonant circular polarized asymmetry energy scans along with associated fits are displayed in the supplementary material, Fig. 17.

SUPPLEMENTARY MATERIAL

See the supplementary material for more information that supports the findings of this work; additional electrochemical data used to generate the overview in the main text; schematics and images of the experimental setups; additional thin film characterization, both before and after electrochemical tests; and additional discussion of results.

ACKNOWLEDGMENTS

The support from the University of Twente in the framework of the tenure track start-up package is gratefully acknowledged. Raymond J. Spiteri and Robert J. Green acknowledge the support from the Natural Sciences and Engineering Research Council of Canada (NSERC) Discovery Grant program. Lucas Korol acknowledges the support from the NSERC CREATE to INSPIRE program. Hans Hilgenkamp , Thijs J. Roskamp, and Carlos M. M. Rosário acknowledge the support from the Dutch Ministry of Education, Culture, and Science (OCW), Program "Materials for the Quantum Age" (QuMat), No. 024.005.006. Magnetocat acknowledges the funding from the European Union's, Horizon 2020 research and innovation program, under Grant Agreement No. 964972 (H2020-FETOPEN-2018-2019-2020-01). Chiara Biz, Mauro Fianchini, and Jose Gracia thank the SpinCat consortium. The authors thank Vadim Ratovskii for fruitful and critical discussion.

AUTHOR DECLARATIONS

Conflict of Interest

The authors have no conflicts to disclose.

Author Contributions

Emma van der Minne: Conceptualization (equal); Data curation (equal); Formal analysis (lead); Investigation (equal); Methodology (equal); Validation (lead); Visualization (lead); Writing – original draft (equal); Writing – review & editing (equal). **Lucas Korol:** Formal

analysis (supporting); Investigation (supporting); Writing – review & editing (supporting). **Lidewij M. A. Krakers:** Formal analysis (supporting); Investigation (supporting). **Michael Verhage:** Formal analysis (supporting); Investigation (supporting); Writing – review & editing (supporting). **Carlos M. M. Rosário:** Formal analysis (supporting); Investigation (supporting). **Thijs J. Roskamp:** Formal analysis (supporting); Investigation (supporting). **Raymond J. Spiteri:** Formal analysis (supporting); Writing – review & editing (supporting). **Chiara Biz:** Formal analysis (supporting); Methodology (supporting); Writing – review & editing (supporting). **Mauro Fianchini:** Formal analysis (supporting); Methodology (supporting); Writing – review & editing (supporting). **Bernard A. Boukamp:** Formal analysis (supporting). **Guus Rijnders:** Methodology (supporting); Writing – review & editing (supporting). **Kees Flipse:** Formal analysis (supporting); Methodology (supporting); Writing – review & editing (supporting). **Jose Gracia:** Formal analysis (supporting); Methodology (supporting); Writing – review & editing (supporting). **Guido Mul:** Conceptualization (supporting); Methodology (supporting); Writing – review & editing (supporting). **Hans Hilgenkamp:** Conceptualization (supporting); Formal analysis (supporting); Methodology (supporting); Writing – review & editing (supporting). **Robert J. Green:** Formal analysis (supporting); Investigation (supporting); Writing – review & editing (supporting). **Gertjan Koster:** Conceptualization (supporting); Methodology (supporting); Supervision (supporting); Writing – review & editing (supporting). **Christoph Baeumer:** Conceptualization (equal); Data curation (supporting); Formal analysis (supporting); Investigation (equal); Methodology (equal); Supervision (lead); Validation (equal); Visualization (equal); Writing – original draft (equal); Writing – review & editing (equal).

DATA AVAILABILITY

The data that support the findings of this study are available within the article and the supplementary material. The data that support the findings of this study are available from the corresponding author upon reasonable request.

REFERENCES

[1]G. W. Crabtree and M. S. Dresselhaus, "The hydrogen fuel alternative," MRS Bull. **33**(4), 421–428 (2008).

[2]Z. Abdin, A. Zafaranloo, A. Rafiee, W. Mérida, W. Lipiński, and K. R. Khalilpour, "Hydrogen as an energy vector," Renewable Sustainable Energy Rev. **120**, 109620 (2020).

[3]D. Karatza, C. Konstantopoulos, S. Chianese, S. Diplas, P. Svec, E. Hristoforou, and D. Musmarra, "Hydrogen production through water splitting at low temperature over Fe_3O_4 pellet: Effects of electric power, magnetic field, and temperature," Fuel Process. Technol. **211**, 106606 (2021).

[4]T. Singh, A. Alhazmi, A. Mohammad, N. Srivastava, S. Haque, S. Sharma, R. Singh, T. Yoon, and V. K. Gupta, "Integrated biohydrogen production via lignocellulosic waste: Opportunity, challenges & future prospects," Bioresour. Technol. **338**, 125511 (2021).

[5]U.S. Department of Energy, "National Clean Hydrogen Strategy and Roadmap," https://www.hydrogen.energy.gov/library/roadmaps-vision/clean-hydrogen-strategy-roadmap (2023), (accessed August 2023).

[6]Fuel Cells and Hydrogen 2 Joint Undertaking. *Hydrogen Roadmap Europe: A Sustainable Pathway for the European Energy Transition* (Publications Office of the European Union, 2019).

[7]D. Antipin and M. Risch, "Trends of epitaxial perovskite oxide films catalyzing the oxygen evolution reaction in alkaline media," J. Phys.: Energy **2**(3), 032003 (2020).

[8]Y. Sun, S. Sun, H. Yang, S. Xi, J. Gracia, and Z. J. Xu, "Spin-related electron transfer and orbital interactions in oxygen electrocatalysis," Adv. Mater. **32**(39), 2003297 (2020).

[9]J. Yao, W. Huang, W. Fang, M. Kuang, N. Jia, H. Ren, D. Liu, C. Lv, C. Liu, J. Xu, and Q. Yan, "Promoting electrocatalytic hydrogen evolution reaction and oxygen evolution reaction by fields: Effects of electric field, magnetic field, strain, and light," Small Methods **4**(10), 2000494 (2020).

[10]X. Ren, T. Wu, Y. Sun, Y. Li, G. Xian, X. Liu, C. Shen, J. Gracia, H. J. Gao, H. Yang, and Z. J. Xu, "Spin-polarized oxygen evolution reaction under magnetic field," Nat. Commun. **12**(1), 2608 (2021).

[11]J. Gracia, R. Sharpe, and J. Munarriz, "Principles determining the activity of magnetic oxides for electron transfer reactions," J. Catal. **361**, 331–338 (2018).

[12]O. V. Khavryuchenko, V. D. Khavryuchenko, and D. Su, "Spin catalysts: A quantum trigger for chemical reactions," Chin. J. Catal. **36**(10), 1656–1661 (2015).

[13]R. R. Nazmutdinov, E. Santos, and W. Schmickler, "Spin effects in oxygen electrocatalysis: A discussion," Electrochem. Commun. **33**, 14–17 (2013).

[14]C. Biz, M. Fianchini, and J. Gracia, "Strongly correlated electrons in catalysis: Focus on quantum exchange," ACS Catal. **11**(22), 14249–14261 (2021).

[15]J. Zou, M. Zheng, Z. Li, X. Zeng, and J. Huang, "Magnetization triggered oxygen evolution reaction enhancement for ferromagnetic materials," J. Mater. Sci.: Mater. Electron. **33**(9), 6700–6709 (2022).

[16]Y. Zhang, P. Guo, S. Li, J. Sun, W. Wang, B. Song, X. Yang, X. Wang, Z. Jiang, G. Wu, and P. Xu, "Magnetic field assisted electrocatalytic oxygen evolution reaction of nickel-based materials," J. Mater. Chem. A **10**(4), 1760–1767 (2022).

[17]F. A. Garcés-Pineda, M. Blasco-Ahicart, D. Nieto-Castro, N. López, and J. R. Galán-Mascarós, "Direct magnetic enhancement of electrocatalytic water oxidation in alkaline media," Nat. Energy **4**(6), 519–525 (2019).

[18]J. Ge, X. Ren, R. R. Chen, Y. Sun, T. Wu, S. J. H. Ong, and Z. J. Xu, "Multi-domain versus single-domain: A magnetic field is not a must for promoting spin-polarized water oxidation," Angew. Chem., Int. Ed. **62**(26), e202301721 (2023).

[19]X. Ren, T. Wu, Z. Gong, L. Pan, J. Meng, H. Yang, F. B. Dagbjartsdottir, A. Fisher, H. J. Gao, and Z. J. Xu, "The origin of magnetization-caused increment in water oxidation," Nat. Commun. **14**(1), 2482 (2023).

[20]T. Sun, Z. Tang, W. Zang, Z. Li, J. Li, Z. Li, L. Cao, J. S. Dominic Rodriguez, C. O. M. Mariano, H. Xu, P. Lyu, X. Hai, H. Lin, X. Sheng, J. Shi, Y. Zheng, Y.-R. Lu, Q. He, J. Chen, K. S. Novoselov, C.-H. Chuang, S. Xi, X. Luo, and J. Lu, "Ferromagnetic single-atom spin catalyst for boosting water splitting," Nat. Nanotechnol. **18**, 763–771 (2023).

[21]T. Wu, X. Ren, Y. Sun, S. Sun, G. Xian, G. G. Scherer, A. C. Fisher, D. Mandler, J. W. Ager, A. Grimaud, J. Wang, C. Shen, H. Yang, J. Gracia, H. J. Gao, and Z. J. Xu, "Spin pinning effect to reconstructed oxyhydroxide layer on ferromagnetic oxides for enhanced water oxidation," Nat. Commun. **12**(1), 3634 (2021).

[22]J. Ge, R. R. Chen, X. Ren, J. Liu, S. J. H. Ong, and Z. J. Xu, "Ferromagnetic–antiferromagnetic coupling core–shell nanoparticles with spin conservation for water oxidation," Adv. Mater. **33**(42), 2101091 (2021).

[23]H. Xu, J. Qi, Y. Zhang, L. Hu, M. Feng, and W. Lü, "Enhanced oxygen evolution reaction via the tunability of spin polarization and electronic states in a flexible van der Waals membranous catalyst," Phys. Chem. Chem. Phys. **25**(30), 20259–20266 (2023).

[24]H. Xu, J. Qi, Y. Zhang, H. Liu, L. Hu, M. Feng, and W. Lü, "Magnetic field-enhanced oxygen evolution reaction via the tuneability of spin polarization in a half-metal catalyst," ACS Appl. Mater. Interfaces **15**(27), 32320–32328 (2023).

[25]V. Gatard, J. Deseure, and M. Chatenet, "Use of magnetic fields in electrochemistry: A selected review," Curr. Opin. Electrochem. **23**, 96–105 (2020).

[26]L. Lin, R. Xin, M. Yuan, T. Wang, J. Li, Y. Xu, X. Xu, M. Li, Y. Du, J. Wang, S. Wang, F. Jiang, W. Wu, C. Lu, B. Huang, Z. Sun, J. Liu, J. He, and G. Sun, "Revealing spin magnetic effect of iron-group layered double hydroxides with enhanced oxygen catalysis," ACS Catal. **13**(2), 1431–1440 (2023).

[27]Y. Ma, T. Wang, X. Sun, Y. Yao, H. Chen, G. Wu, C. Zhang, and Y. Qin, "Enhanced oxygen evolution of a magnetic catalyst by regulating intrinsic magnetism," ACS Appl. Mater. Interfaces **15**(6), 7978–7986 (2023).

[28]R. R. Chen, Y. Sun, S. J. H. Ong, S. Xi, Y. Du, C. Liu, O. Lev, and Z. J. Xu, "Antiferromagnetic inverse spinel oxide $LiCoVO_4$ with spin-polarized channels for water oxidation," Adv. Mater. **32**(10), 1907976 (2020).

[29]P. Huang, M. Meng, G. Zhou, P. Wang, W. Wei, H. Li, R. Huang, F. Liu, and L. Liu, "Dynamic orbital hybridization triggered spin-disorder renormalization via super-exchange interaction for oxygen evolution reaction," Proc. Natl. Acad. Sci. U. S. A. **120**(21), e2219661120 (2023).
[30]Z. Sun, L. Lin, J. He, D. Ding, T. Wang, J. Li, M. Li, Y. Liu, Y. Li, M. Yuan, B. Huang, H. Li, and G. Sun, "Regulating the spin state of Fe^{III} enhances the magnetic effect of the molecular catalysis mechanism," J. Am. Chem. Soc. **144**(18), 8204–8213 (2022).
[31]Y. Tong, Y. Guo, P. Chen, H. Liu, M. Zhang, L. Zhang, W. Yan, W. Chu, C. Wu, and Y. Xie, "Spin-state regulation of perovskite cobaltite to realize enhanced oxygen evolution activity," Chem **3**(5), 812–821 (2017).
[32]J. Pan, T. Li, and Y. Shan, "Spin-dependent reconstruction induced by surface symmetry breaking in manganese spinel oxides toward acidic oxygen evolution reaction," Phys. Status Solidi RRL **17**(12), 2300124 (2023).
[33]M. Huijben, L. W. Martin, Y. H. Chu, M. B. Holcomb, P. Yu, G. Rijnders, D. H. A. Blank, and R. Ramesh, "Critical thickness and orbital ordering in ultrathin $La_{0.7}Sr_{0.3}MnO_3$ films," Phys. Rev. B **78**(9), 094413 (2008).
[34]C. Biz, J. Gracia, and M. Fianchini, "Review on magnetism in catalysis: From theory to PEMFC applications of 3*d* metal Pt-based alloys," Int. J. Mol. Sci. **23**(23), 14768 (2022).
[35]M. L. Weber and F. Gunkel, "Epitaxial catalysts for oxygen evolution reaction: Model systems and beyond," J. Phys.: Energy **1**(3), 031001 (2019).
[36]C. Baeumer, J. Li, Q. Lu, A. Y. L. Liang, L. Jin, H. P. Martins, T. Duchoň, M. Glöß, S. M. Gericke, M. A. Wohlgemuth, M. Giesen, E. E. Penn, R. Dittmann, F. Gunkel, R. Waser, M. Bajdich, S. Nemšák, J. T. Mefford, and W. C. Chueh, "Tuning electrochemically driven surface transformation in atomically flat $LaNiO_3$ thin films for enhanced water electrolysis," Nat. Mater. **20**(5), 674–682 (2021).
[37]J. Hemberger, A. Krimmel, T. Kurz, H. A. Krug von Nidda, V. Y. Ivanov, A. A. Mukhin, A. M. Balbashov, and A. Loidl, "Structural, magnetic, and electrical properties of single-crystalline $La_{1-x}Sr_xMnO_3$ $(0.4 < x < 0.85)$," Phys. Rev. B **66**(9), 094410 (2002).
[38]J. Gracia, J. Munarriz, V. Polo, R. Sharpe, Y. Jiao, J. W. H. Niemantsverdriet, and T. Lim, "Analysis of the magnetic entropy in oxygen reduction reactions catalysed by manganite perovskites," ChemCatChem **9**(17), 3358–3363 (2017).
[39]M. Verhage, E. van der Minne, E. M. Kiens, L. Korol, R. J. Spiteri, G. Koster, R. J. Green, C. Baeumer, and K. Flipse, "A complementary experimental study of epitaxial $La_{0.67}Sr_{0.33}MnO_3$ to identify morphological and chemical disorder," arXiv:2311.00504 (2023).
[40]S. Macke, A. Radi, J. E. Hamann-Borrero, A. Verna, M. Bluschke, S. Brück, E. Goering, R. Sutarto, F. He, G. Cristiani, M. Wu, E. Benckiser, H. U. Habermeier, G. Logvenov, N. Gauquelin, G. A. Botton, A. P. Kajdos, S. Stemmer, G. A. Sawatzky, M. W. Haverkort, B. Keimer, and V. Hinkov, "Element specific monolayer depth profiling," Adv. Mater. **26**(38), 6554–6559 (2014).
[41]L. Li, Y. Ji, Z. Diao, J. Zhang, and Z. Liao, "Toward ultrathin ferromagnetic metal of (110) $La_{2/3}Sr_{1/3}MnO_3$ thin films," Appl. Phys. Lett. **117**(12), 122404 (2020).
[42]F. Tsui, M. C. Smoak, T. K. Nath, and C. B. Eom, "Strain-dependent magnetic phase diagram of epitaxial $La_{0.67}Sr_{0.33}MnO_3$ thin films," Appl. Phys. Lett. **76**(17), 2421–2423 (2000).
[43]E. Dagotto, T. Hotta, and A. Moreo, "Colossal magnetoresistant materials: The key role of phase separation," Phys. Rep. **344**(1–3), 1–153 (2001).
[44]L. Yin, C. Wang, Q. Shen, and L. Zhang, "Strain-induced Curie temperature variation in $La_{0.9}Sr_{0.1}MnO_3$ thin films," RSC Adv. **6**(98), 96093–96102 (2016).
[45]G. Li, H. D. Zhou, S. J. Feng, X. J. Fan, X. G. Li, and Z. D. Wang, "Competition between ferromagnetic metallic and paramagnetic insulating phases in manganites," J. Appl. Phys. **92**(3), 1406–1410 (2002).
[46]S. Fletcher, "Tafel slopes from first principles," J. Solid State Electrochem. **13**(4), 537–549 (2009).
[47]S. Czioska, K. Ehelebe, J. Geppert, D. Escalera-López, A. Boubnov, E. Saraçi, B. Mayerhöfer, U. Krewer, S. Cherevko, and J. D. Grunwaldt, "Heating up the OER: Investigation of IrO_2 OER catalysts as function of potential and temperature**," ChemElectroChem **9**(19), e202200514 (2022).
[48]L. Chen, Z. Wang, G. Wang, H. Guo, M. Saghayezhian, Z. Liao, Y. Zhu, E. W. Plummer, and J. Zhang, "Surface and interface properties of $La_{2/3}Sr_{1/3}MnO_3$ thin films on $SrTiO_3$ (001)," Phys. Rev. Mater. **3**(4), 044407 (2019).
[49]G. Shibata, K. Yoshimatsu, E. Sakai, V. R. Singh, V. K. Verma, K. Ishigami, T. Harano, T. Kadono, Y. Takeda, T. Okane, Y. Saitoh, H. Yamagami, A. Sawa, H. Kumigashira, M. Oshima, T. Koide, and A. Fujimori, "Thickness-dependent ferromagnetic metal to paramagnetic insulator transition in $La_{0.6}Sr_{0.4}MnO_3$ thin films studied by x-ray magnetic circular dichroism," Phys. Rev. B **89**(23), 235123 (2014).
[50]Z. Liao, N. Gauquelin, R. J. Green, S. Macke, J. Gonnissen, S. Thomas, Z. Zhong, L. Li, L. Si, S. Van Aert, P. Hansmann, K. Held, J. Xia, J. Verbeeck, G. Van Tendeloo, G. A. Sawatzky, G. Koster, M. Huijben, and G. Rijnders, "Thickness dependent properties in oxide heterostructures driven by structurally induced metal–oxygen hybridization variations," Adv. Funct. Mater. **27**(17), 1606717 (2017).
[51]S. Macke, J. E. Hamann-Borrero, R. J. Green, B. Keimer, G. A. Sawatzky, and M. W. Haverkort, "Dynamical effects in resonant X-ray diffraction," Phys. Rev. Lett. **117**(11), 115501 (2016).
[52]H. Pan, X. Jiang, X. Wang, Q. Wang, M. Wang, and Y. Shen, "Effective magnetic field regulation of the radical pair spin states in electrocatalytic CO_2 reduction," J. Phys. Chem. Lett. **11**(1), 48–53 (2020).
[53]J. Suntivich, K. May, H. Gasteiger, J. Goodenough, and Y. Shao-Horn, "A perovskite oxide optimized for oxygen evolution catalysis from molecular orbital principles," Science **334**(6061), 1383–1386 (2011).
[54]Y. Liang, K. Banjac, K. Martin, N. Zigon, S. Lee, N. Vanthuyne, F. A. Garcés-Pineda, J. R. Galán-Mascarós, X. Hu, N. Avarvari, and M. Lingenfelder, "Enhancement of electrocatalytic oxygen evolution by chiral molecular functionalization of hybrid 2D electrodes," Nat. Commun. **13**(1), 3356 (2022).
[55]A. Vadakkayil, C. Clever, K. N. Kunzler, S. Tan, B. P. Bloom, and D. H. Waldeck, "Chiral electrocatalysts eclipse water splitting metrics through spin control," Nat. Commun. **14**(1), 1067 (2023).
[56]W. Mtangi, F. Tassinari, K. Vankayala, A. Vargas Jentzsch, B. Adelizzi, A. R. A. Palmans, C. Fontanesi, E. W. Meijer, and R. Naaman, "Control of electrons' spin eliminates hydrogen peroxide formation during water splitting," J. Am. Chem. Soc. **139**(7), 2794–2798 (2017).
[57]P. Reith, X. Renshaw Wang, and H. Hilgenkamp, "Analysing magnetism using scanning SQUID microscopy," Rev. Sci. Instrum. **88**(12), 123706 (2017).
[58]J. R. Kirtley, M. B. Ketchen, K. G. Stawiasz, J. Z. Sun, W. J. Gallagher, S. H. Blanton, and S. J. Wind, "High-resolution scanning SQUID microscope," Appl. Phys. Lett. **66**(9), 1138–1140 (1995).
[59]S. Anantharaj and S. Noda, "*iR* drop correction in electrocatalysis: Everything one needs to know!," J. Mater. Chem. A **10**(17), 9348–9354 (2022).
[60]A. Lasia, *Electrochemical Impedance Spectroscopy and Its Applications* (Springer New York, New York, 2014).
[61]D. G. Hawthorn, F. He, L. Venema, H. Davis, A. J. Achkar, J. Zhang, R. Sutarto, H. Wadati, A. Radi, T. Wilson, G. Wright, K. M. Shen, J. Geck, H. Zhang, V. Novák, and G. A. Sawatzky, "An in-vacuum diffractometer for resonant elastic soft x-ray scattering," Rev. Sci. Instrum. **82**(7), 073104 (2011).